Detailed Simulations of the DLR Auto-Igniting Pulsed Jet Experiment

E. Inanc[a,*], J. T. Lipkowicz[a], A. M. Kempf[a]

[a]*Chair of Fluid Dynamics, Institute for Combustion and Gasdynamics (IVG), University of Duisburg-Essen, Germany*

Abstract

Numerical simulations of an auto-igniting pulsed jet in a vitiated co-flow experiment by DLR (German Aerospace Center) are conducted by highly-resolved large-eddy simulations using direct chemistry with an augmented reduced mechanism. The experiments consist of two operation modes: continuous injection used for code-verification and pulsed injection utilized for fundamental investigation of auto-ignition dynamics. Initially, reference one-dimensional self-igniting counter-flow flames are investigated. Then, a grid convergence study has been performed. It is shown that even a coarser grid would be sufficient to describe the ignition chemistry since the ignition kernel appears at low velocities and fuel-lean conditions in zones of low scalar dissipation rates. For the statistically steady jet, numerical predictions are in a very good agreement with the experiments, giving confidence in the applied models. For the pulsed jet, all of the predicted ignition delay times and locations are in the range of the experimental observations. Time-resolved statistics reveal that thermochemical properties of the gas in a pulsed jet achieve states that are impossible to reproduce in laminar conditions. For further analysis, hydroxyl and formaldehyde are chosen as a marker for the established flame and for the ignition, respectively. In laminar conditions, these two species are perfectly correlated. However, the unsteady dynamics of the pulsed jet invalidates the correlation between the minor species chemistry prior to ignition. This yields the discrepancy in the auto-ignition delay time and the location of the ignition kernel between different pulses, as the thermochemical state needed for the ignition occurs in a random manner.

Keywords:
Pulsed Jets, Large-Eddy Simulation, Direct Chemistry, Ignition, Scalar Dissipation Rate.

1. Introduction

In many combustion systems, ignition occurs after the fuel is impulsively injected into the combustion chamber. To optimize these systems, ignition and combustion must be rigorously studied [1, 2, 3], an overview of recent works is given by Mastorakos [4]. Ignition and flame chemistry in pulsed auto-igniting jet flames are challenging to consider due to the many degrees of freedom and the resulting computational or experimental cost. Moreover, the wide range of time and length scales of mixing and chemistry make pulsed cases costly to simulate, even without considering reaction kinetics, as demonstrated by various groups [5, 6].

As ignition depends strongly on chemistry, numerical investigations of ignition require detailed chemical mechanisms that are coupled preferably with direct numerical simulations (DNS) [7]. However for the pulsed jet, the computational costs have to be reduced, hence, only a few attempts have been made with tabulated chemistry that relies on a few control parameters [8]. Such simulations have shown that the ignition dynamics of pulsed jets can be approximated by highly resolved large-eddy simulations (LES) [8]. However, the question remains how well the tabulated chemistry can resolve the complex chemical process, and if a relevant physical understanding can be extracted from such simulations.

Advanced high-speed imaging has made it possible to determine the ignition delay time and location of the ignition kernel and the subsequent evolution of the early flame [9, 10, 11, 12, 13]. A recent example is the DLR (German Aerospace Center) pulsed jet experiment [12]. Compared to the jet in hot co-flow (JHC) cases [14, 15], this experiment toggles the fuel valve to generate cycle statistics. The DLR jet experiment has been modeled initially by Fiotakis et al. [16] under steady conditions. Their interest has been the distance of the stabilized flame from the injector nozzle. Another attempt has been made by our group using tabulated chemistry to show the cycle-to-cycle variations of the ignition [8]. As the employed tabulation method reduced the dimensionality of the chemistry, the correlations between the scalars were biased. Recently, Liu et al. [17] have performed an LES with detailed chemistry, where they observed premixed-mode combustion during the stabilized flame propagation.

The motivation of this work is to test the suitability of the available numerical models applicable for ignition investigations in pulsed jets with an aim to identify the origin of statistical variations in auto-ignition dynamics. To do that, the present work reproduces the DLR experiments with the LES using direct chemistry. These well-defined experiments provide a reliable data-set for statistically steady and pulsed injection variations, which help to test, develop and improve the numerical models.

*Corresponding author
Email address: eray.inanc@uni-due.de (E. Inanc)

2. Experiment

In the auto-igniting pulsed jet in a vitiated co-flow experiment by DLR Stuttgart [12], a methane jet at 290 K and 177.5 ms^{-1} was injected into a 4 ms^{-1} co-flow at 1490 K, which consisted of fuel-lean hydrogen/air ($\phi = 0.465$) combustion products at ambient pressure. A summary is given in Table 1. The injector tube had a diameter of $D = 1.5$ mm, and the jet-Reynolds number was 16,000. The stoichiometric mixture fraction was $Z_{ST} = 0.0297$.

This experiment consisted of two operation modes: steady and pulsed injection. In the steady mode, the fuel was continuously injected to achieve a lifted flame, and the mean and RMS of fuel mass fractions and the temperature were obtained using Raman/Rayleigh diagnostics. In the pulsed mode, the fuel-inlet valve was opened and closed to achieve a pulsed jet, and ignition statistics were established by high-speed planar laser-induced fluorescence imaging. The pulses were separated by two seconds to flush the left-over residuals. A total of 300 pulse-cycles were sampled.

3. Numerical modeling

The simulations were conducted with the in-house LES/DNS code PsiPhi [5, 8, 18, 19]. The Favre-filtered governing equations for mass, momentum, (a total of 19) species mass fractions and absolute enthalpy were solved with a low-storage explicit third-order Runge-Kutta scheme in the pressure-based formulation. A density-based formulation was not considered here, as a previous comparison of compressible and incompressible simulations [8] showed a negligible effect of compressibility in this case, even at relatively high subsonic Mach numbers, as the flow is dominated by shear rather than by stagnation points. The convective fluxes of scalars were determined by a TVD scheme (with CHARM [20] limiter), and by a second-order central scheme for momentum. A power-law velocity profile was imposed at the inlet, superimposed with synthetic turbulence [21, 22].

Direct chemistry with the augmented reduced mechanism (ARM) by Lu and Law [23] was employed with 19 transported species, 11 quasi-steady-state species and 15 lumped reactions. Extensive validation of this mechanism has been presented [23]. A unity Lewis number assumption was employed.

An algebraic model was used to estimate the scalar dissipation rate (SDR) χ of the mixture fraction Z. The sub-grid part of $\tilde{\chi}$ was modeled with a simplified version of the method by Girimaji and Zhou [24] with molecular D and turbulent diffusivities D_t as $\tilde{\chi} = 2(D + D_t)\nabla\tilde{Z}\nabla\tilde{Z}$.

The unresolved fluxes of momentum and species mass fractions were estimated from an eddy-viscosity approach with a turbulent Schmidt number of 0.7, based on Nicoud's σ-model [25]. The reaction-rate source terms do not include a sub-grid contribution, which will be justified in the section on grid convergence.

The steady reference case with direct chemistry at lower-resolution (SDl) was simulated for 75 ms of real-time, where sampling was started after 25 ms (1.5 co-flow advection times). For the pulsed cases, a linear function was assumed for ramping up and down the fuel mass flow over 0.5 ms (ramp up function might affect the outcome but testing is prohibitive at the current cost of the simulations). In between, the fuel was continuously injected for 10 ms. After another 39 ms, the fuel stream was ramped up again, so that each simulated cycle lasted 50 ms – enough to avoid interference between the pulses. In the lower-resolution transient computation with direct chemistry (TDl), 311 ms were computed – corresponding to six pulse-cycles. For the higher-resolution transient simulation with direct chemistry (TDh), only 61 ms could be afforded, corresponding to two pulse-cycles. The first cycle in each case was not evaluated. A summary of the simulations is given in Table 2.

The computational domain was a 65x36x36 mm^3 box containing an equidistant Cartesian-grid and included the final 3 mm of the fuel injector tube. The time step width was limited by a convective CFL number of 0.3. The grid resolutions of 0.1 mm (lower-resolution) and 0.05 mm (higher-resolution) resulted in 80 million and 637 million cells, respectively, leading to a computational time requirement of 40 million core hours on the fine grid with direct chemistry.

4. Results

4.1. Grid resolution

Pulsed jet predictions by the LES must resolve the mixing near the injector at upstream and the flame chemistry at downstream locations where the ignition would occur. To demonstrate the suitability of the grid, a convergence study is first presented for the steady case. The radial mean and root-mean-square (RMS) fuel mass fraction $\tilde{Y}_{CH_4}$ and temperature $\tilde{T}$ from the different grids are presented at resolutions of 0.25 mm, 0.15 mm and 0.1 mm in Fig. 1.

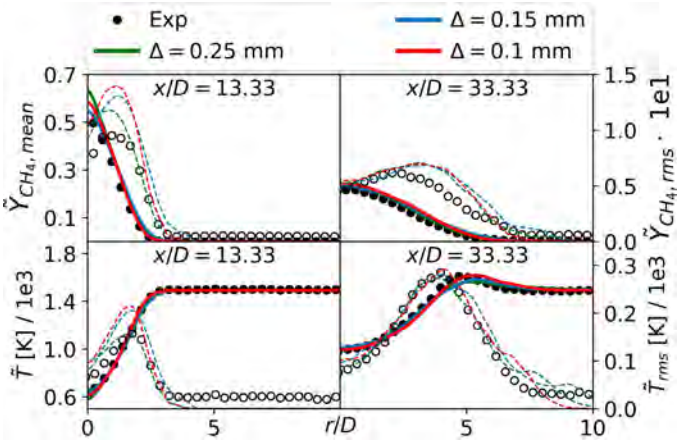

Figure 1: Radial profiles of mean (filled dots and straight lines) and RMS (empty dots and dashed lines) fuel mass fraction $\tilde{Y}_{CH_4}$ (upper row) and temperature $\tilde{T}$ (bottom row) at two axial locations for three grid resolutions and experiment of the statistically steady jet.

The 0.25 and 0.15 mm grid simulations share the same simulation parameters as SDl with the 0.1 mm grid. Comparing the predicted fuel mass fractions to the experiments in Fig. 1, the

Table 1: Thermochemical state of the fuel and the co-flow of DLR experiment [12].

Jet	$\overline{U}_f$ [m/s]	Z_{ST}	T_o [K]	**Co-flow**	$\overline{U}_o$ [m/s]	X_{N_2}	X_{O_2}	X_{H_2O}	X_{OH}	T_f [K]
	177.5	0.0297	290		4.0	0.712	0.102	0.178	0.82E-6	1490

Table 2: Details of the steady case with direct chemistry at low-resolution (SDl), and the transient cases with direct chemistry at low (TDl) and high resolution (TDh).

Case	**SDl**	**TDl**	**TDh**
Injections	cont.	6-cycle	2-cycle
#Cells	80 M	80 M	637 M
Δ/mm	0.10	0.10	0.05
time/ms	75	311	61
#CPU	11,016	11,016	93,600
CPUh	4 M	4 M	40 M

width of the jet is well estimated even using a coarse grid of 0.25 mm, whereas the center-line fuel-mass fraction at 20 mm is slightly overestimated. The temperature profiles agree well with the experiment, the maximum temperature at $x/D = 33.33$ (at $r/D = 5$) is slightly under-predicted for both the 0.25 and 0.15 mm grids. Further upstream, the temperature fluctuations in the mixing layer are slightly under-predicted on the coarse grid but agree well when a finer grid is employed. This grid study indicates that even a medium grid of 0.15 mm could be sufficient for this study.

Due to the lack of suitable validation data for the pulsed case, the grid resolution requirement is determined using a different approach: the grid resolution considered well-resolved for the steady case (0.1 mm) is refined by a safety factor of two to ensure sufficient resolution for the pulsed case. The resulting resolution of 0.05 mm is also sufficient to resolve the Kolmogorov scales in the region where ignition occurs ($\eta_K = 0.17$ mm) estimated as in the maxing layer at $x/D = 20$ with $\eta_K = [\nu^3 l_t/(u')^3]^{0.25}$ from the kinematic viscosity ν and the integral length scale l_t. This 0.05 mm resolution is further evaluated using two LES resolution criteria, knowing that these must be treated with care: the sub-grid activity parameter $s = \mu_t/(\mu + \mu_t)$ by Geurts et al. [26] and the LES index of resolution quality '$LESIQ$' by Celik et al. [27] as presented in Fig. 2.

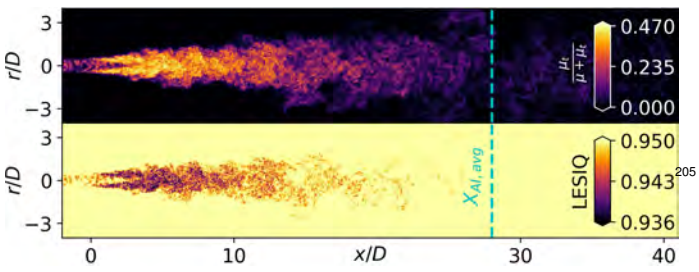

Figure 2: Contour plots of the sub-grid activity parameter [26] (top) and the LES index of resolution quality '$LESIQ$' [27] (bottom) from the TDh case with 0.05 mm grid. Cyan dashed-line marks the average ignition height in the DLR experiment [12].

In TDh, the sub-grid activity parameter s [26] does not exceed 0.47, which indicates that most of the flow scales are well-resolved. Where the AI is expected (around $x/D \approx 28$), this parameter approaches to zero. The $LESIQ$ is a function of the sub-grid activity with an upper limit of 0.9524 (sic) for a turbulent viscosity of zero, defined as $LESIQ = (1 + 0.05[(\mu + \mu_t)/\mu]^{0.53})^{-1}$. In the TDh simulations, upstream locations achieve the $LESIQ$ value of at least 0.936, whereas downstream locations exceed 0.95. These values imply a very high resolution, but it should be noted that these quality estimators must not be trusted on their own, as they strongly depend on the turbulence models and the numerical schemes. In the present simulations, these parameters justify that no significant sub-grid contribution is detected or considered by the simulation that could have affected the results.

The grid resolution can also be compared to similar simulations: Doan et al. [28] recently performed DNS of ignition of mild combustion in shear layers using a grid resolution of 0.02 mm, where the turbulent Reynolds number was 97. They specified that there were about 30 grid points inside the smallest chemical thickness. A similar DNS study by Göktolga et al. [29] used a 0.04 mm grid for a much higher turbulent Reynolds number of 192. Proch et al. [30] performed flame-resolved simulations of turbulent stratified jet flames using a grid with 0.1 mm spacing for a turbulent Reynolds number of 563. Our simulations have a high turbulent Reynolds number of 790 directly in the fuel inlet, but, where ignition occurred, as low as 116. Thus, using a resolution of 0.05 mm appears to be sufficient to resolve the chemical source terms in their Favre filtered form with at least five grid points in the stably burning flame.

The resolution requirements for the present partially premixed flames and auto-ignition (AI) dynamics have been analyzed a priori using one-dimensional simulations. An extensive overview is given in Appendices A and B, a summary is given here: the partially premixed reaction zones can reasonably be described using a 0.05 mm grid resolution, even at very high strain rates (Fig. A.21). A resolution finer than 0.2 mm yields the correct AI delay time in the reference diffusion flames (Fig. B.23b).

4.2. Steady jet

Figure 3 shows the mixture fraction $\tilde{Z}$, the corresponding scalar dissipation rate (SDR) $\tilde{\chi}$ and the temperature fields from SDl. These contour plots provide a brief overview of the simulations. High SDR values are present in the mixing layer, whereas, in downstream locations, the mixing layer is thicker with much lower SDR values. Figure 3c shows a flame lift-off length of $x/D = 30$, but an increased (instantaneous) temperature is already visible at $x/D = 25$ in Fig. 3d.

Radial profiles for means and RMS of fuel mass fraction $\tilde{Y}_{CH_4}$ and temperature $\tilde{T}$ are shown in Figs. 4 and 5. At 20 mm, the fuel mass fraction is slightly over-predicted towards the center-

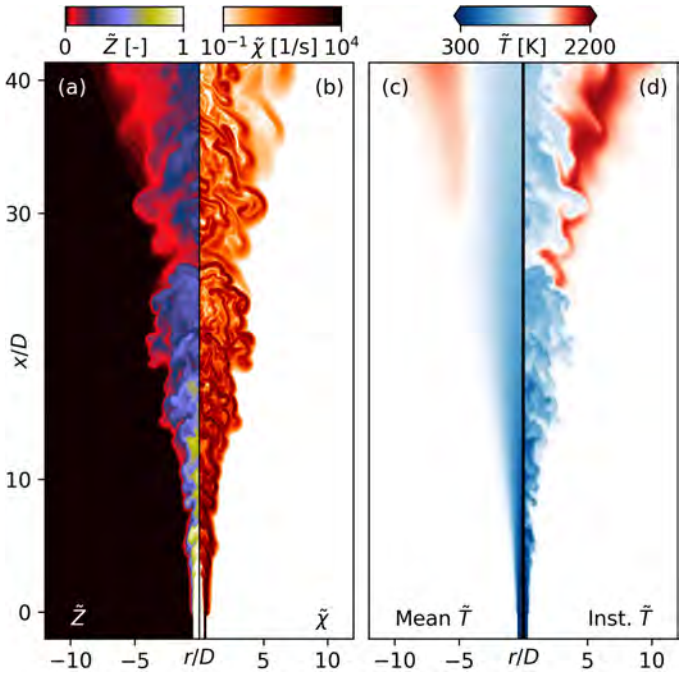

Figure 3: Instantaneous mixture fraction $\tilde{Z}$ (a) and SDR $\tilde{\chi}$ (b) with mean (c) and instantaneous (d) temperature $\tilde{T}$ contours from SDl.

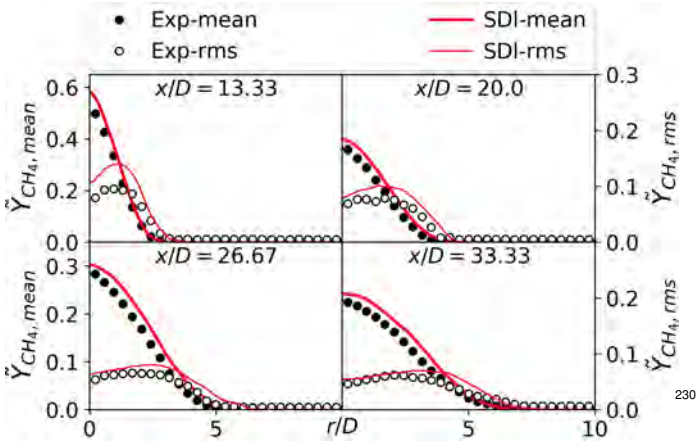

Figure 4: Radial profiles of mean and RMS of methane mass fraction $\tilde{Y}_{CH_4}$ for SDl.

line, where the fluctuations are accordingly over-predicted. Further downstream, the predictions achieve a very good agreement to the experiments [31]. The temperature predictions, however, are in very good agreement with the experiments. The lift-off lengths for both SDl and experiments are almost the same.

Radial profiles for normalized mean and RMS of hydroxyl mass fraction $\tilde{Y}^*_{OH} = \tilde{Y}_{OH}/\tilde{Y}_{OH,max}$ are shown in Fig. 6. The experiments obtained the mean OH profiles from averaging single snapshots after the flame stabilized in 300 different cycles. The OH data-set is given in particle number densities in $1/m^3$ (personal communication [31]). Therefore, the values are normalized with their maximum values for comparison. The accurate predictions of these normalized mean and RMS OH profile

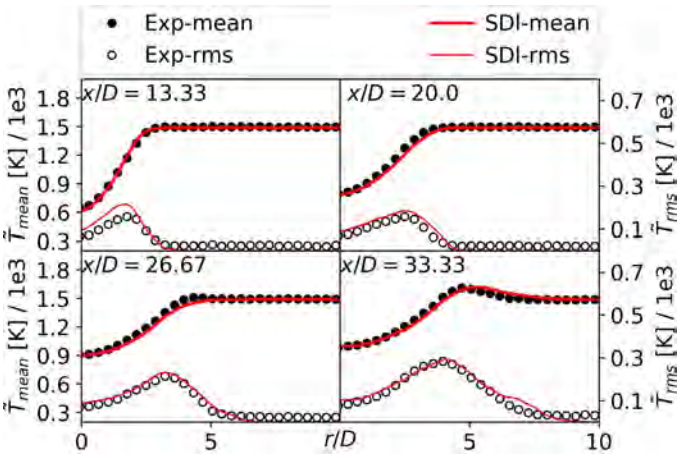

Figure 5: Radial profiles of mean and RMS of temperature $\tilde{T}$ for SDl.

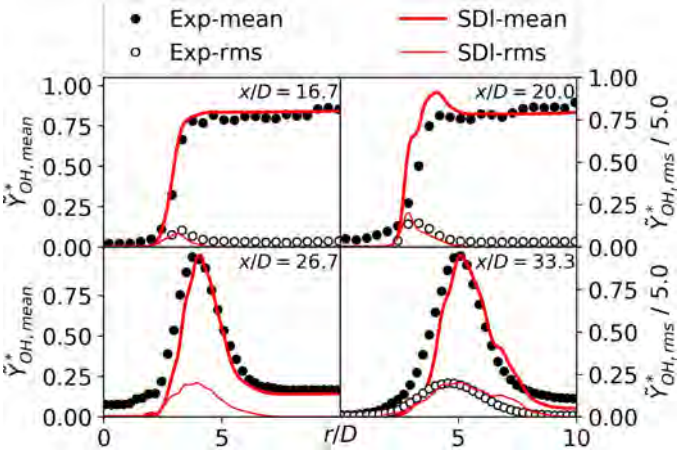

Figure 6: Radial profiles of normalized mean and RMS of OH mass fraction $\tilde{Y}^*_{OH}$ for SDl.

shapes point to correct flame propagation speeds and reaction rates. The pulsed mode in the following sections uses the confidence in numerical models gained from the agreement in the steady mode.

4.3. Pulsed jet

In the absence of turbulence, the auto-ignition (AI) delay time τ_{AI} depends on the local composition, the initial temperature of the fuel/oxidizer mixture and the local scalar gradients. Reference one-dimensional auto-igniting laminar counter-flow simulations using the conditions of the DLR experiment [12] were conducted a priori to determine the most-reactive mixture fraction Z_{MR}, critical scalar-dissipation rate χ_c and ignition scalar-dissipation rate χ_{AI}. Further details are given in Appendix B.

With the computational setup validated in the steady reference case and proven to yield accurate results, the pulsating case is investigated with direct chemistry at high-resolution. The temporal evolution of the impulsively starting jet in TDh is illustrated by SDR fields in Fig. 7, which also includes the axial plots of the highest SDR values in each x-plane. The leading

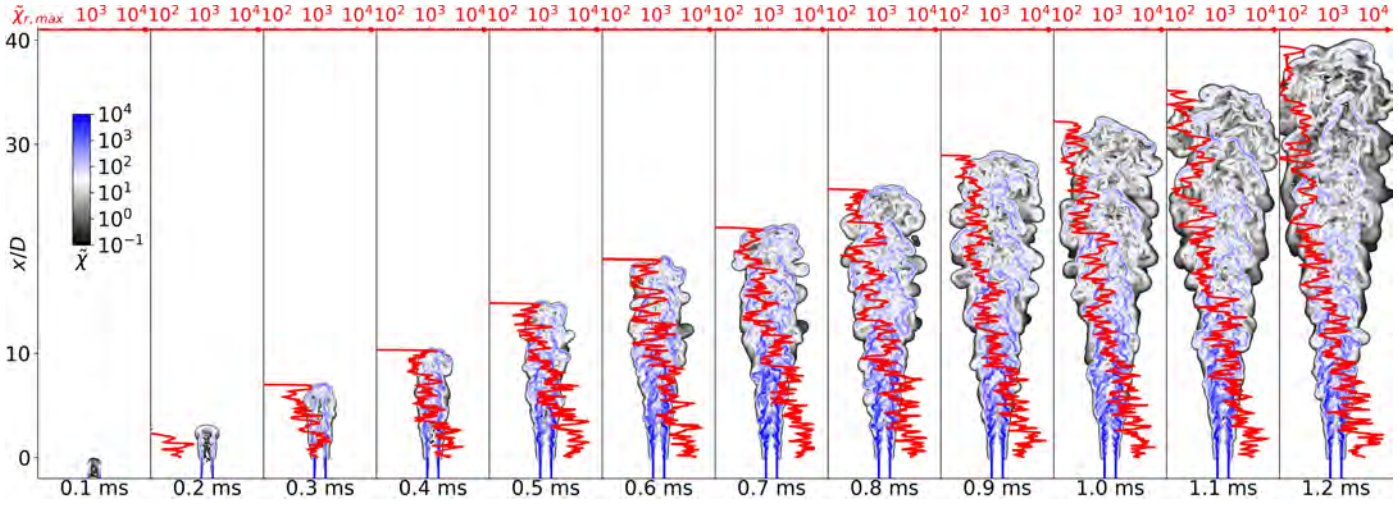

Figure 7: Temporal evolution of the jet illustrated by snapshots of SDR $\tilde{\chi}$ from the high-resolution simulation (TDh). Red lines give the maximum SDR in radial direction.

vortex ring, typical for cold starting jets [5], is less pronounced here due to the low co-flow density. The outer layer characterized by high SDR marks the mixing layer (blue contours) between the fuel-jet and the co-flow. After 1 ms, the zones with low SDR consist of a relatively homogeneous mixture, establishing a favorable condition for the jet to ignite. However, most early ignition kernels fail, and sustained combustion only occurs after 1.9 ms. The axial plots show that the SDR values peak near the nozzle exit.

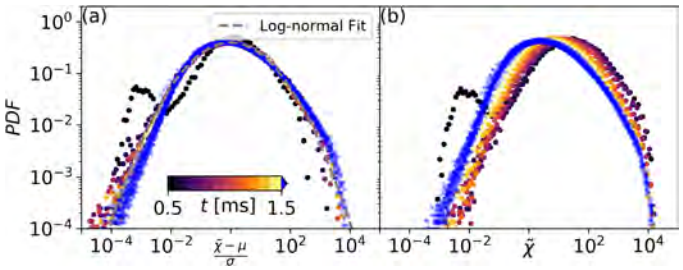

Figure 8: The PDFs of the normalized (a) and non-normalized (b) SDR calculated at different times (from TDh). The line denotes a log-normal fit. ($t > 1.5$ ms have blue lines).

The time evolution of the normalized and non-normalized probability density function (PDF) of the SDR are presented in Fig. 8 for TDh. From 0.7 ms, the normalized PDFs follow the log-normal fit, just as in non-reactive transient jets [5]. The PDF shifts towards smaller SDR values with time, as illustrated in Fig. 8b, due to dissipation. Only at very early times, significant deviations from the log-normal distribution are observed, with an increased probability of very small SDR ($\tilde{\chi} < 0.01$) values.

The joint probability density function (JPDF) of mixture fraction and SDR is shown in Fig. 9. The JPDF is used to analyze the statistical dependence between the mixture fraction and its dissipation rate, which are commonly assumed independent for non-premixed flames [32]. It is shown in Fig. 9 that SDR and the mixture fraction in the LES are independent.

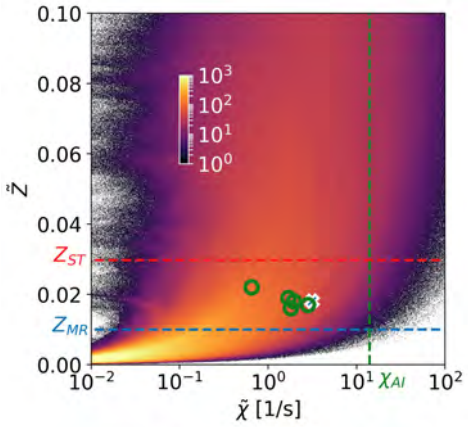

Figure 9: Joint probability density function (JPDF) of mixture fraction and SDR immediately prior to the ignition at 2 ms for TDh. White/blue and green markers indicate the states at ignition for a single TDh cycle and five TDl cycles, respectively.

Small SDR values are conditionally expected in extreme fuel-lean (and fuel-rich) mixtures since the mixture fraction distribution in a mixing layer of a non-premixed flame resembles an error function. This also concludes that a statistical analysis based on SDR would not be biased towards a conditional mixture fraction range.

4.4. Auto-ignition (AI) in cycle variations

The evolution of an ignition kernel is visualized in Fig. 10, superimposed on the SDR field. The ignition kernel is marked by an iso-line at $T_{AI} = 1800$ K. Ignition begins with the formation of a singular temperature kernel in a lean mixture at $Z = 0.018$ ($Z_{MR} = 0.01$), very low SDR ($\tilde{\chi} = 0.6$ s^{-1}) and low velocity ($\tilde{U}_i = 12.4$ ms^{-1}). This indicates that the ignition kernel grew almost in the co-flow. The ignition kernel spreads towards rich mixtures $\tilde{Z} = 0.025$ and larger SDR ($\tilde{\chi} = 3.1$ s^{-1}) at 2.0 ms.

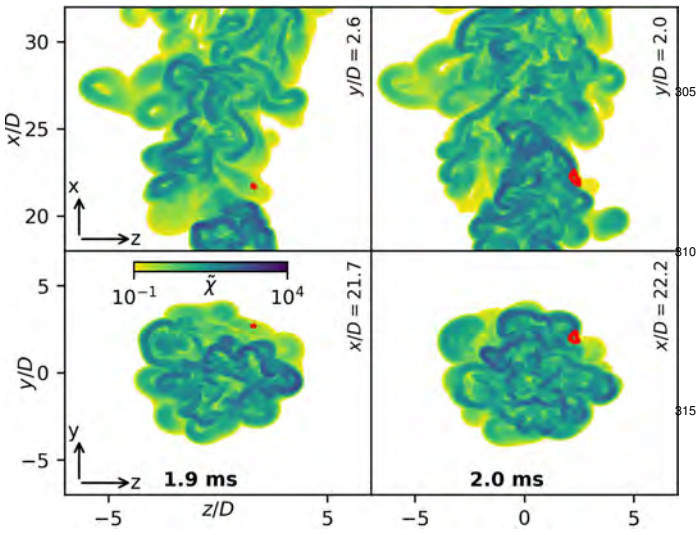

Figure 10: Snapshots of SDR field during an ignition event for TDh, showing the early ignition spot (red iso-line) at 1.9 ms and the growing ignition kernel at 2 ms. The planes for visualization are chosen to intersect the kernel.

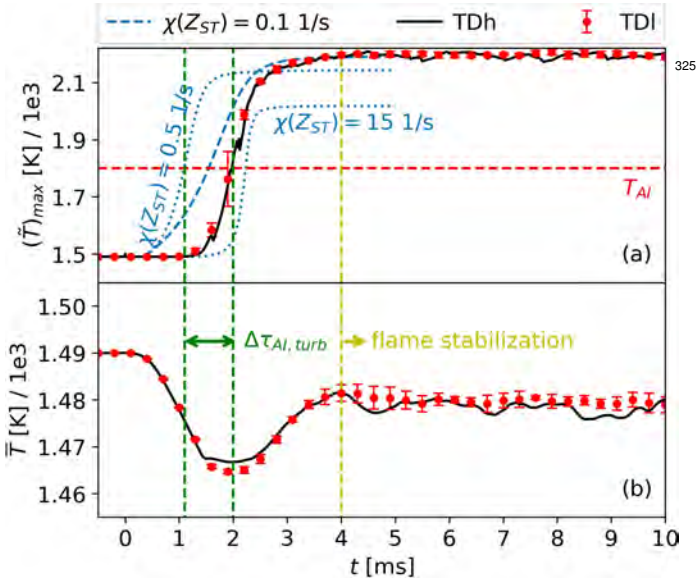

Figure 11: Maximum (a) and volume-averaged (b) temperature over the cycle time. The error-bars indicate the standard deviation of each cycle.

Maximum and volume-averaged temperatures over the cycle-time shown in Fig. 11 are compared to three reference one-dimensional igniting counter-flow simulations. The maximum temperature starts to increase at around 1.5 ms and stabilizes after 4 ms, indicating a stabilized jet flame. The different cycles from TDl vary most at 4.5 ms, as illustrated by the error bars in Fig. 11a, and agree well with the single cycle from TDh with the finest grid. This indicates that the results are reproducible on the different grids. Short temporary drops in the maximum temperature point to local quenching events due to turbulent strain.

In the LES, AI occurs at an SDR of 0.5 s^{-1}, resulting in temperatures of up to 2210 K. Comparing the maximum temperature evolution between the LES and the one-dimensional reference case (with the same SDR as the LES), the ignition is delayed by 0.95 ms (denoted as $\Delta\tau_{AI}$). However, the temperature curves of the LES and the one-dimensional cases are very similar apart from such high-temperatures. These high temperatures of the LES are only achieved in one-dimensional reference flames at a low SDR of 0.1 s^{-1}. This maximum temperature difference can be explained as the gas undergoing ignition would spread to regions with lower SDR, hence, high temperatures from the reference case at an SDR of 0.1 s^{-1} are achieved later, at 2.4 ms. In the LES, it is plausible for a configuration with a much shorter delay $\Delta\tau_{AI} \approx 0$ ms (i.e. slow injection of the fuel) to achieve a maximum temperature curve as in the present case. But, this requires the ignition kernel to be in a local zone with relatively large SDR represented with the one-dimensional case of $\tilde{\chi} = 15$ s^{-1} – unlikely to happen in the present transient case. Apart from the variation of SDR in the ignition kernel and the short temporary temperature drops, the thermo-chemical properties in pulsed jets resemble one-dimensional reference cases – particularly important for combustion modeling assumptions. Figure 11b shows how the injection of cold fluid causes an initial drop in the volume-averaged temperature prior to ignition. The flame stabilizes at 4ms, which is in line with the observations by the experimentalists [12].

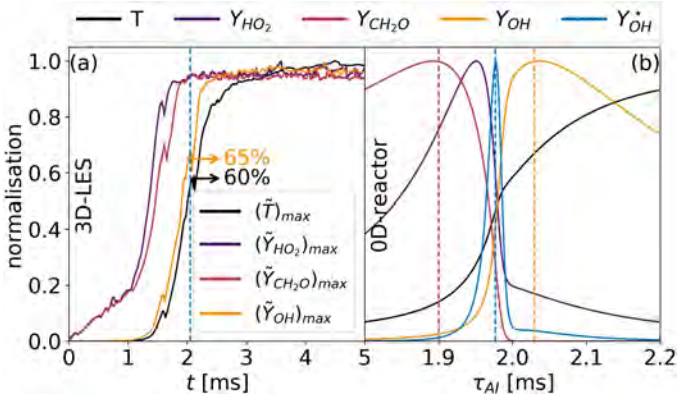

Figure 12: Normalized maximum temperature and species mass fractions over the cycle time (a) for TDh. The same normalized scalars over the AI delay time from zero-dimensional homogeneous reactor simulation (b) using Cantera [33] with GRI-3.0 mechanism [34], which is extended with excited OH* species.

Figure 12a shows normalized hydroperoxyl HO_2, formaldehyde CH_2O and OH mass fractions relative to temperature over the cycle time. The profiles obtained from the LES are compared against a reference homogeneous reactor using GRI-3.0 [34] with Cantera [33] in Fig. 12b. The initial reactor conditions are chosen from the mixing line at $Z = 0.011$. The excited OH* chemistry is included according to [35]. In the LES, the HO_2 and CH_2O species form simultaneously, followed by the OH species and temperature with 1 ms delay. A brief drop in all these quantities at 1.5 ms is likely caused by a quenching event caused by strain. Contrary to the LES, the reactor results show that HO_2 forms later than CH_2O. This could be attributed to the enhanced physical interaction of flow in pulsed jets that affects the reaction kinetics.

The AI delay times have been determined for each of the 300

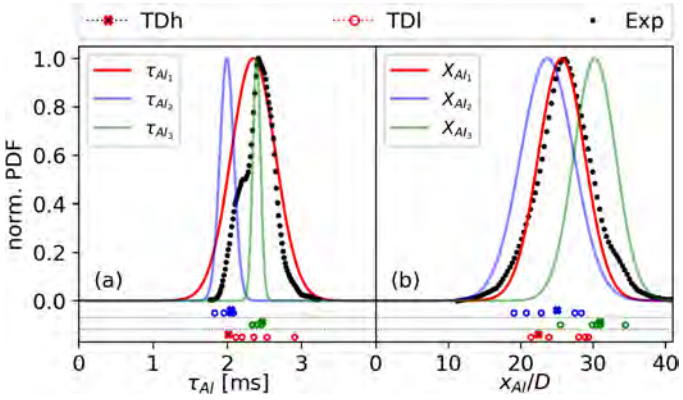

Figure 13: Predicted ignition delay times (a) and distance from the burner exit (b) shown as circle markers. A fitted Gaussian PDF to the predicted samples and normalized PDF of experiments are given.

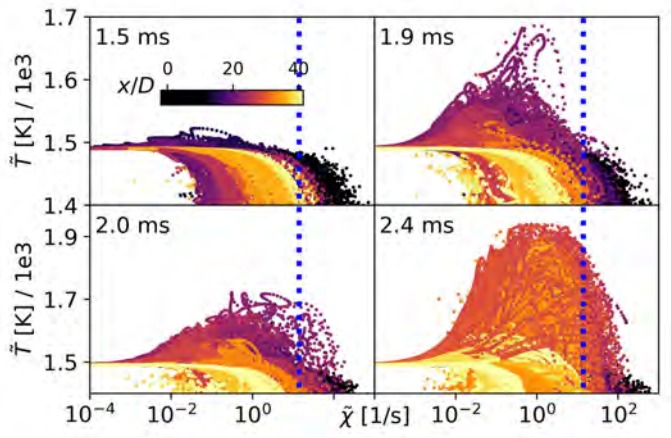

Figure 14: Scatter plots of temperature $\tilde{T}$ over SDR $\tilde{\chi}$ for different times colored by the axial location from TDh. The blue line marks the ignition SDR χ_{AI} determined in the reference simulations.

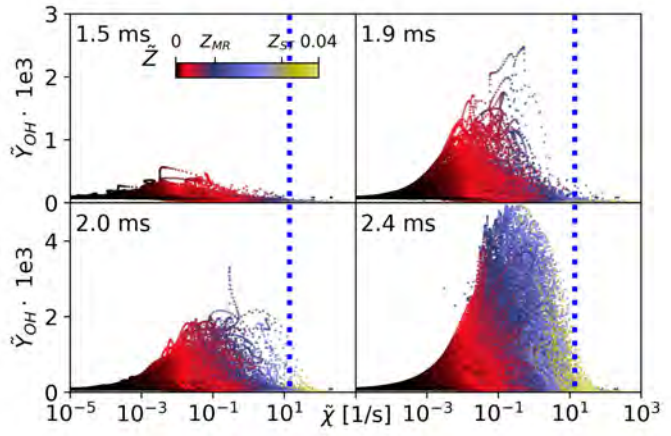

Figure 15: Scatter plots of OH mass fraction over SDR $\tilde{\chi}$ for different times colored by the mixture fraction $\tilde{Z}$ from TDh. The blue line marks the ignition SDR χ_{AI} determined in the reference simulations.

pulses observed in the experiment, defined as the time when light-emission from OH* reaches its maximum value. These auto-ignition delay times lead to the distribution shown in Fig. 13a over time and in Fig. 13b over axial location. In the simulations, OH* concentrations are not available, thus, alternative criteria for the AI delay time were required. A first criterion is based on the peak mass fraction of formaldehyde CH_2O, which leads the OH* concentration by 0.1 ms (as shown in Fig. 12b), and yields τ_{AI_1}. A second criterion is based on the temperature exceeding T_{AI} for the first time (τ_{AI_2}). The third criterion is the time when the maximum OH mass fraction is reached for the first time in the flame (τ_{AI_3}), which is delayed by 0.04 ms from the OH* concentration (Fig. 12b).

The predictions from the TDl and TDh cases are shown as markers. Three Gaussian distributions fitted to the means and standard deviations of τ_{AI_α} and X_{AI_α} from the simulations are compared against the distribution from the experiment. For the first AI delay time definition τ_{AI_1}, the width and the location of the predicted distributions of both τ_{AI_1} and X_{AI_1} are in good agreement with the experiments. A reasonable agreement is also achieved for the other criteria ($\tau_{AI_{2-3}}$ and $X_{AI_{2-3}}$), indicating that the tested ignition definitions are interchangeable accepting a slight deviation.

The mixture fraction and the SDR immediately prior to the ignition is marked on the previous Fig. 9. All of the cycles from both TDl and TDH ignite in fuel-lean mixtures, but, slightly richer than the most reactive mixture fraction Z_{MR}, as marked on the Fig. 9. The cycle variations are clustered to $0.5 < \tilde{\chi} < 5\ \mathrm{s}^{-1}$, in agreement with the a priori estimations in Fig. B.23a.

4.5. Pre-ignition chemistry

Further analysis will consider the effect of the SDR of the mixture fraction. The largest SDR value with a reasonable AI delay is denoted as the ignition SDR $\chi_{AI} = 14\ \mathrm{s}^{-1}$, highlighted in Appendix B. Figures 14 to 17 show scatter plots of temperature and mass fractions of OH, CH_2O and HO_2 over the SDR $\tilde{\chi}$. Since the formaldehyde CH_2O and hydroperoxyl HO_2 species appear immediately prior to ignition [4] and hydroxyl species appear prior to the stabilized flame, CH_2O/HO_2 and OH are used as markers for before and after ignition, respectively.

Figure 14 shows minor heating at small SDR values after 1.5 ms already, but temperatures above ignition temperature are only seen after 2 ms or immediately prior to ignition. This temperature rise occurs at around $x/D = 25$ (purple contours), presumably indicating the location of the pre-ignition kernel. After the ignition at 2.4 ms, high temperatures are observed further downstream ($x/D > 30$) and at higher SDR values. The high temperatures at SDR beyond χ_{AI} cannot result from ignition but from the heat diffusion (Soret effect) or an increase of SDR after the ignition due to strain. Figure 15 shows that OH statistics converge to a Gaussian distribution. Local minor OH concentration increases before the ignition at 1.5 ms. Prior to ignition at 1.9 ms, some high OH concentrations are evident beyond χ_{AI} in the fuel-rich side. The highest OH concentrations prior to ignition are found near the most reactive mixture fraction.

Figures 16 and 17 show high CH_2O and HO_2 concentrations prior to ignition over a wider range of SDR than OH distribution. Prior to ignition at 1.9 ms, high CH_2O and HO_2 concentrations appear near the most reactive mixture fraction at an axial

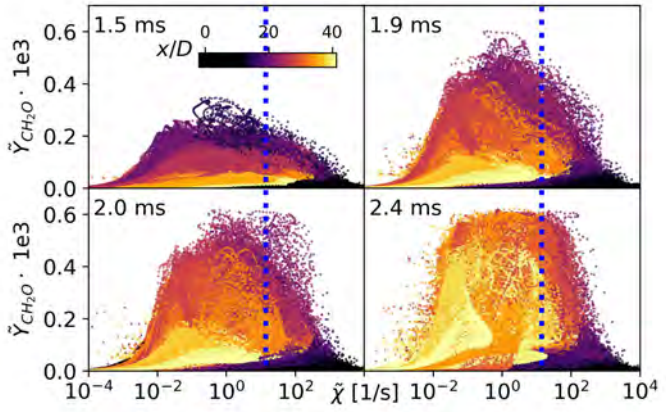

Figure 16: Scatter plots of CH_2O mass fraction over SDR $\tilde{\chi}$ for different times colored by the axial distance from TDh. The blue line marks the ignition SDR χ_{AI} determined in the reference simulations.

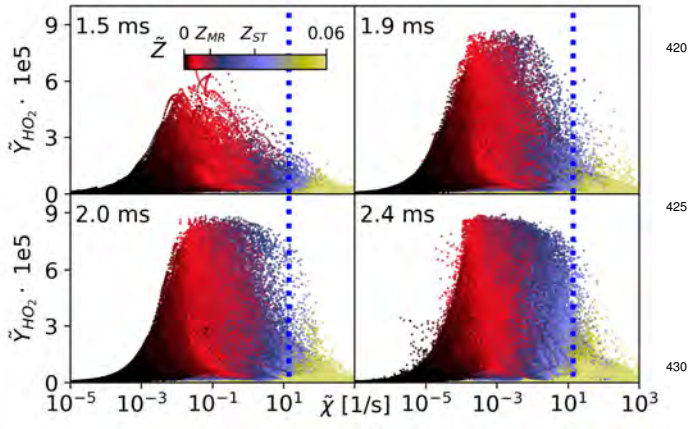

Figure 17: Scatter plots of HO_2 mass fraction over SDR $\tilde{\chi}$ for different times colored by the mixture fraction $\tilde{Z}$ from TDh. The blue line marks the ignition SDR χ_{AI} determined in the reference simulations.

distance of the ignition ($x > 25D$). It is clearly noticeable that the high CH_2O and HO_2 concentrations are evident beyond χ_{AI} near the nozzle. The species beyond χ_{AI} appear in any AI delay time and are found in extreme fuel-lean conditions ($Z < 0.001$). A notable difference is the SDR dependency of HO_2 is a factor of ten smaller than CH_2O.

Each species has a lower and upper SDR limit depending on the species time scales that cannot be estimated from the reference cases. Some species such as OH are more sensitive to the SDR than others such as CH_2O or HO_2, where less sensitive species appear far beyond χ_{AI}. It is evident that the s-curve (Fig. B.22b) does not include the complete spectrum of the thermochemical states in a pulsed jet for both lower and upper SDR limits, especially for the minor species related to the ignition (CH_2O/HO_2) that appear downstream where the unsteady mixing in pulsed jets occurs.

4.6. Post-ignition chemistry

Under laminar conditions, OH and CH_2O species are correlated, as a function of the AI delay time and SDR. The next part

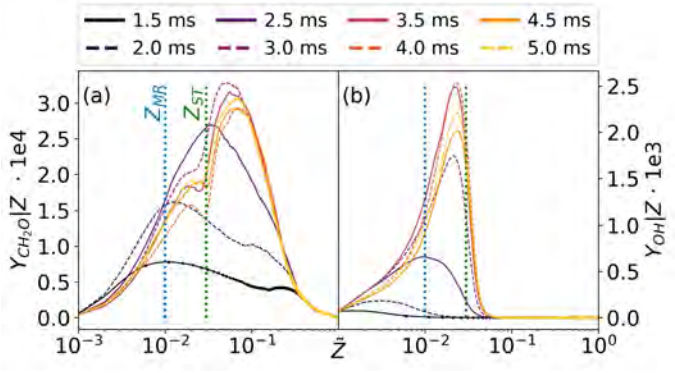

Figure 18: Time evolution of the conditional means of mass fractions of CH_2O (a) and OH (b) of TDh. Blue and green dashed lines represent the most reactive and stoichiometric mixture fractions Z_{MR} and Z_{ST}, respectively.

of the analysis focuses on the statistical deviations of the pulsed jets from the reference laminar conditions by cross-comparing these two aforementioned species. Figure 18 shows the time evolution of the mean CH_2O and OH mass fractions conditioned on the mixture fraction. The peak CH_2O distribution at 1.5 ms is located near the most reactive mixture Z_{MR}, whereas positive mean CH_2O values are observable over a wide range of mixture fraction. At the time of ignition, the CH_2O profile shape is a Gaussian distribution. However, over the AI delay time, the initial bi-modal distribution shape with positive skew transforms into the same distribution but with a negative skew. Meanwhile, OH shows a monotonic increase of the mean OH concentrations until 4 ms, appearing in the very lean side and shifting towards Z_{ST}. The mean OH distribution shows negatively skewed Gaussian distribution with platykurtic and leptokurtic properties before and after the ignition, respectively. The widths of the species distributions indicate the weaker and stronger correlations for CH_2O and OH over the mixture fraction, respectively.

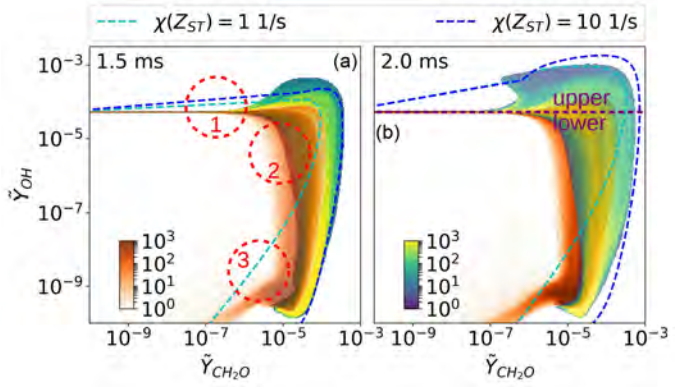

Figure 19: Two JPDF of CH_2O and OH mass fractions with two reference cases at two different times. Red contours show the JPDF conditioned on upstream half of the domain ($x < 25D$) and green/yellow contours are conditioned on the downstream half of the domain ($x > 25D$).

The statistical differences between the pre- and post-ignition chemistry are investigated with JPDF of CH_2O and OH mass fractions in Fig. 19 with two AI delay times of 1.5 and 2 ms.

The red and green JPDF contours indicate upstream ($x < 25D$) and downstream ($x > 25D$) locations, respectively. Two reference one-dimensional simulation results at similar AI delay times to the LES are given as well. Following any reference simulation line, CH_2O and OH mass fractions show upper and lower branches, as indicated in 19b. The zone denoted with circle-1 in the upper branch reveals that the CH_2O in the LES only occurs after reaching a threshold of OH mass fraction, contrary to reference simulations. The zone marked as circle-2 shows the probability of observing these two species that are not reproducible from the reference simulations. This zone is dominated with the species from the LES found upstream at 1.5 ms. The zone marked as circle-3, however, contains states of two species that the LES never achieves. It is evident that the correlations between CH_2O and OH upstream are not statistically consistent with the reference simulations, contrary to the downstream locations that show closer agreements to the chemical states from the reference simulations. This demonstrates the effect of unsteady mixing on chemical kinetics.

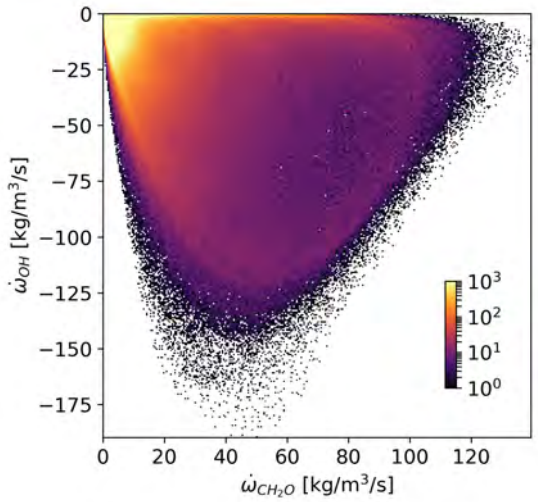

Figure 20: JPDF of CH_2O and OH reaction rates $\dot{\omega}$ at immediately prior to ignition of 2 ms.

In the final part, the JPDF of the CH_2O and OH reaction rates are presented in Fig. 20 at 2 ms immediately prior to the ignition. Excluding the samples with very low reaction rates ($|\dot{\omega}| < 10$ kgm^{-3}s^{-1}), only a very weak correlation between CH_2O and OH reaction rate can be observed, noting that different AI delay times are omitted for brevity and produce the same outcome. It is clearly evident that the AI delay time difference between the LES and reference simulations $\Delta\tau_{AI}$ is caused by the unsteady mixing dynamics of a pulsed jet that affect the pre-ignition chemistry that is strongly perceived in minor species correlations.

5. Conclusions

The numerical simulations of the auto-igniting pulsed jet in a vitiated co-flow experiment [12] with the direct chemistry approach showed a very good agreement between the predictions and the experiments for both versions of this experiment: continuous and pulsed injection of the fuel. It was demonstrated initially that the employed grid resolution to resolve the unsteady mixing and ignition chemistry was sufficient. Then, the mixture fraction and the scalar-dissipation rate were analyzed to justify the unbiased statistics when using either one of these scalars.

The time and space resolved ignition kernel showed that the AI favored a mixing layer closer to the hot and diffusive co-flow stream. The definition of the AI relied on certain thresholds, hence, alternative definitions applicable for pulsed jets were tested, which yielded similar outcomes with only minor differences. Using a limited amount of samples, it was demonstrated that the AI delay time and the location of the ignition kernel varied greatly for different pulse-cycles. The AI in pulsed jets was compared to the reference one-dimensional laminar auto-igniting flames, where it was shown that the cycle-deviations of ignition dynamics were not reproducible, but could only be estimated stochastically.

It was found that the statistical variations between the cycles in pulsed jets were caused by the unsteady mixing affecting the reaction kinetics prior to the ignition. The analysis of minor species showed that the pulsed jet chemistry achieved thermo-chemical states that were not reproducible with reference one-dimensional simulations. The statistical distribution of minor species related to the ignition (i.e. CH_2O) over both mixture fraction and scalar dissipation rate (SDR) spaces strongly deviated from the reference cases. Similar deviations were observed for the minor species related to the stabilized flame (i.e. OH), however, in a much lesser extent. Hence, the cross-correlations between the minor species were lost. These deviations were mostly observed in upstream locations where the unsteady mixing was dominant. However, the post-ignition statistics in downstream locations were in agreement with the reference simulations. It is concluded that the unsteady flow prior to ignition affected the reaction kinetics (dominantly) of the ignition-related species. This caused a delay for the pulsed jet to find a state that permits the ignition, which then occurred in a randomized manner.

6. Acknowledgments

The authors are grateful for the financial support by DFG (Proj. No.: 393710272, KE 1751/13-1) and the Gauss Center High-Performance computing grant on Hazel Hen, Stuttgart (44141 GCS-JFLA).

Appendix A. One-dimensional strained premixed flames

The resolution requirements for the partially premixed reaction zones typically found in this work can be estimated a priori using one-dimensional simulations. Figure A.21 presents CH_2O mass fraction and its reaction-rate profiles over physical and progress variable spaces using different grid resolutions from reference premixed laminar counter-flow flames in one-dimension under heavy compressible strain. These premixed

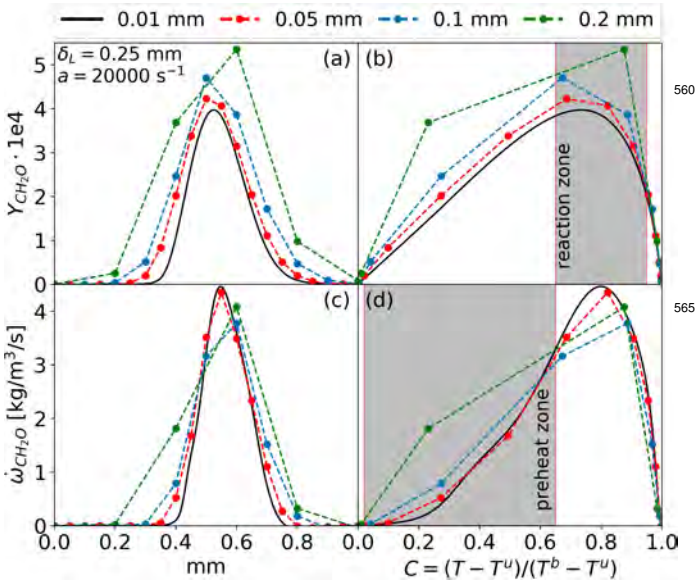

Figure A.21: Four one-dimensional counter-flow stoichiometric methane/air flame simulations under a compressible strain of $a = 20000$ s^{-1} with different grid sizes using Cantera [33]. Mass fraction (a,b) and reaction-rate (c,d) of CH_2O are presented over the physical space (a,c) and progress variable (b,d). Each circle marks a computational cell.

flames are simulated with Cantera [33] using GRI-3.0 [34] at stoichiometric conditions.

The compressible strain is introduced to the simulations by injecting fresh fuel and air mixture at 300 K from the left boundary and fully burnt products of this mixture from the right boundary. The mass flow rates are adjusted such that an extreme compressible strain of 20,000 s^{-1} is achieved, which yields a reaction zone thickness $\delta_l = 0.25$ mm computed from $\delta_L = (T^b - T^u)/max(\nabla T)$, where T^b and T^u denote burnt and unburnt gas temperatures, respectively. The progress of the combustion is tracked with a progress variable C computed from the temperature profile as $C = (T - T^u)/(T^b - T^u)$, where $C = 0$ denotes fresh reactants and $C = 1$ represents fully burnt products. The inner reaction zone has a C value between 0.65 and 0.95 and the preheat zone ranges between $0.02<C<0.65$ [36]. This simulation is repeated for different equivalence ratios, where $\phi = 1$ result is shown for brevity since the reaction zones are the smallest. It should be noted that the fuel stratification effects could further decrease the reaction zone thickness, but not drastically as reported before [37, 38].

The coarser grid in Fig. A.21 with 0.2 mm over-predicts the CH_2O concentrations. This probably affects the rest of the species and the propagation speeds as the complete progress variable space has just three points. The increase of the resolution by a factor of two to 0.1 mm improves the results quite well, where now the inner reaction zone consists of two grid points. The resolution of 0.05 mm, which is also the resolution employed in this work, further increase the agreement, where the inner reaction zone has now four grid points (and the preheat zone has three grid points). Similarly, a good agreement can be achieved for the reaction rate of CH_2O using a grid finer than 0.1 mm. Since the strain rates are much lower where the ignition kernel emerges in the LES, it is a good estimate that 0.05 mm resolution would be sufficient to resolve the thin reaction zones.

Appendix B. One-dimensional igniting flames

In the absence of turbulence, the auto-ignition (AI) delay time τ_{AI} depends on the local composition and initial temperature of the fuel/oxidizer mixture, as long as the local scalar gradients are low. Reference one-dimensional auto-igniting laminar counter-flow simulations using the boundary conditions from DLR experiments [12] with the GRI-3.0 mechanism [34] using FlameMaster [39] are presented a priori.

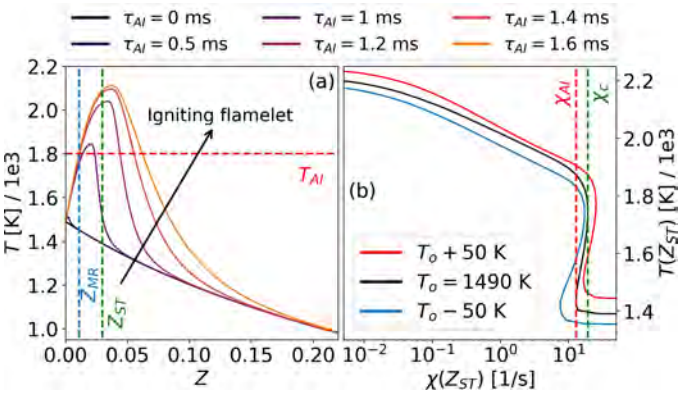

Figure B.22: Temperature profile of igniting counter-flow one-dimensional simulations over mixture fraction (a). Each line represents a different AI delay time, as denoted in the legend. Most reactive Z_{MR} and stoichiometric Z_{ST} mixture fractions are shown with blue and green dashed lines, respectively. Ignition temperature threshold of 1800 K is shown with red dashed line. Three s-curves of this case are presented (b) for three co-flow temperatures. Ignition χ_{AI} and critical χ_c SDRs are shown with red and green dashed lines, respectively.

Figure B.22a shows the temperature profile of a one-dimensional igniting counter-flow simulation over the mixture fraction. This representative case uses a stoichiometric SDR $\chi(Z_{ST}) = 1$ s^{-1}, which is the local SDR value in the stoichiometric mixture fraction Z_{ST}. A priori analysis yields the most-reactive mixture fraction Z_{MR}, which is the corresponding mixture fraction when the flame ignites. In Fig. B.22a, a small temperature rise on extreme fuel-lean conditions ($Z < 0.001$) is observable for the AI delay time of 0.5 ms, which cannot be considered as the most-reactive mixture fraction since the maximum local temperature is too low. Hence, a threshold temperature is needed to indicate if the mixture is ignited. For this work, a temperature threshold of 1800 K is employed, denoted as T_{AI}. The composition that passes the threshold T_{AI} has the most-reactive mixture fraction of $Z_{MR} = 0.01$ and AI delay time of $\tau_{AI} = 1$ ms. The maximum temperature is shifted to fuel-richer mixtures than Z_{MR} and Z_{ST} due to the diffusion of heat. Since a counter-flow configuration with much lower SDR would yield the kinetics to dominate the diffusive fluxes, Z_{MR} and T_{AI} are determined from the case with much lower SDR, in this case, 0.01 s^{-1} of the stoichiometric composition $\chi(Z_{ST})$.

The s-curve for diffusion type flames [40] of this configuration is given in Fig. B.22b. The s-curve is derived from

several completely ignited counter-flow one-dimensional simulations, where the temperature and SDR values on the stoichiometric mixture fraction Z_{ST} are plotted against each other. The upper, middle and lower branches of the s-curve are visible. The transition of the s-curve from the upper branch to the middle branch happens on a specific SDR value referred to as critical SDR χ_c, which in this case has a fairly low value of $\chi_c = 19\ \mathrm{s}^{-1}$. The configurations that have larger SDR than this critical SDR χ_c would not burn due to flow time scales being too short for chemistry to advance [40]. However, the simulations with slightly lower SDR than χ_c have an extreme long AI delay time τ_{AI}. Thus, a new SDR parameter is introduced here as the ignition SDR χ_{AI}, which is the largest SDR value before the τ_{AI} reaches 3 ms, which is the longest delay time duration observed in the DLR experiments [12]. Figure B.22b presents s-curves for the same cases but with co-flow temperatures 50 K above and below to emphasize the neglectable sensitivity of χ_{AI} (and χ_c) with regards to variations.

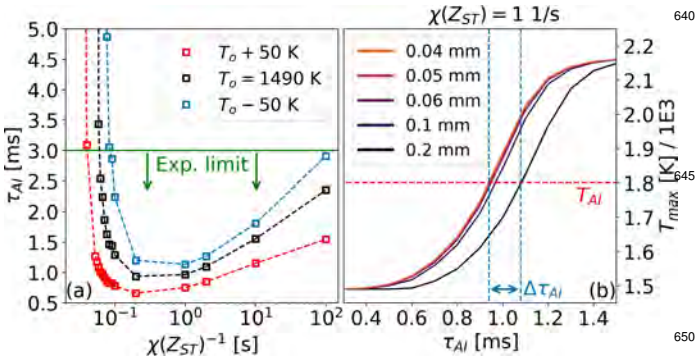

Figure B.23: AI delay time τ_{AI} over inverse of SDR (a) of the stoichiometric composition. Each square marks τ_{AI} of a particular one-dimensional simulation with different SDR. Two additional curves are given for the simulations with different co-flow temperatures. Green dashed-line is the longest delay time in DLR experiments [12]. AI delay time τ_{AI} over maximum temperature T_{max} (b) for the one-dimensional simulation with different grid sizes is presented for the case with an SDR value of 1 s^{-1} of the stoichiometric composition.

The sensitivity of the AI delay times on the SDR is shown in Fig. B.23a by presenting τ_{AI} over the inverse of the SDR of the stoichiometric composition $\chi(Z_{ST})$. The τ_{AI} of one-dimensional cases are obtained when the maximum temperature reaches T_{AI} threshold. Figure B.23a presents results from 15 different calculations, where each τ_{AI} is marked individually with a square marker. The AI delay time growths towards infinity immediately after reaching the critical SDR χ_c, where the ignition SDR is estimated as $\chi_{AI} = 14\ \mathrm{s}^{-1}$. The simulation with an SDR of 5 s^{-1} has the shortest τ_{AI}. As mentioned earlier, simulations with lower SDR $\chi < 1$ ignite rather slow due to insufficient mixing. Figure B.23a also contains two additional curves with 50 K varied co-flow temperatures, however, χ_{AI} for these cases only slightly varies deviates from the main curve. Meanwhile, τ_{AI} greatly varies for the cases with low $\chi = 0.01$.

The one-dimensional counter-flow simulations in FlameMaster [39] are solved in mixture fraction space as described by Peters [40] using a presumed error function as the grid. This error function is adjusted so that the SDR profile has the desired value on the stoichiometric mixture fraction. Using a central differencing scheme on the partial derivative of the mixture fraction ∇Z yields $\Delta_Z/\Delta(Z)$, where mixture fraction spacing Δ_Z is constant throughout the simulations in FlameMaster [39]. Hence, the SDR equation can be rewritten as

$$\chi = 2D(\nabla Z)^2 = 2D\left(\frac{\Delta_Z}{\Delta(Z)}\right)^2 \tag{B.1}$$

The physical cell spacing $\Delta(Z)$ can be approximated from the local diffusivity $D_{Z,T}$ and local SDR $\chi(Z)$ values on the local mixture fraction, as in Eq. (B.2).

$$\Delta(Z) = \sqrt{\frac{2D_{Z,T}}{\chi(Z)}}\Delta_Z \tag{B.2}$$

Figure B.23b presents the maximum temperature over time for a reference one-dimensional simulation with $\chi(Z_{ST}) = 1\ \mathrm{s}^{-1}$ with different mixture fraction spacing Δ_Z. The spacing Δ_Z is adjusted such that the physical cell spacing on the most reactive mixture fraction Z_{MR} has a value ranging from 0.04 to 0.2 mm, approximated using Eq. (B.2). Since the diffusivity $D_{Z,T}$ varies with the increase of the local temperature, the local diffusivity at the ignition temperature T_{AI} is chosen. It should also be noted that different $\chi(Z_{ST})$ yields the same outcome since Δ_Z and $\sqrt{\chi(Z)}$ term in Eq. (B.2) are linked with the presumed error function, and $D_{Z,T}$ term does not depend on the SDR.

The ignition is delayed by $\Delta\tau_{AI}$ if the extreme fuel-lean conditions are not resolved, as can be seen from 0.2 mm case in Fig. B.23b that has a delay of 1 ms. However, the ignition still happens even when using a coarse grid. The AI delay times τ_{AI} are similar for the simulations that use a grid size lower than 0.1 mm.

The a priori analysis of one-dimensional cases suggests that the ignition should occur on a most-reactive mixture fraction Z_{MR} of 0.01, which is on the fuel-lean side. The ignition, however, should happen on an SDR that is lower than the ignition SDR χ_{AI} and higher than the extreme low SDR ($\chi > 0.01\ \mathrm{s}^{-1}$). The local temperature of the ignition kernel is only important if the ignition happens on the extreme low SDR ($\chi < 0.1\ \mathrm{s}^{-1}$). Finally, the cell spacing required to resolve the auto-ignition should also be as low as 0.1 mm.

References

[1] R. Cabra, T. Myhrvold, J. Y. Chen, R. W. Dibble, A. N. Karpetis, R. S. Barlow, Simultaneous laser Raman-Rayleigh-LIF measurements and numerical modeling results of a lifted turbulent H2/N2 jet flame in a vitiated coflow, Proc. Combust. Inst. 29 (2) (2002) 1881–1888.

[2] P. Domingo, L. Vervisch, D. Veynante, Large-eddy simulation of a lifted methane jet flame in a vitiated coflow, Combust. Flame 152 (3) (2008) 415–432.

[3] E. Oldenhof, M. Tummers, E. Van Veen, D. Roekaerts, Ignition kernel formation and lift-off behaviour of jet-in-hot-coflow flames, Combust. Flame 157 (6) (2010) 1167–1178.

[4] E. Mastorakos, Ignition of turbulent non-premixed flames, Prog. in En. Comb. Sci. 35 (1) (2009) 57–97.

[5] E. Inanc, M. T. Nguyen, S. Kaiser, A. M. Kempf, High-resolution LES of a starting jet, Comp. Fluids 140 (2016) 435–449.

[6] M. van Reeuwijk, P. Salizzoni, G. Hunt, J. Craske, Turbulent transport and entrainment in jets and plumes: A LES study, Phy. Rev. Fluids 1 (7) (2016) 074301.

[7] E. Mastorakos, T. A. Baritaud, T. J. Poinsot, Numerical simulations of autoignition in turbulent mixing flows, Combust. Flame 109 (1) (1997) 198–223.

[8] E. Inanc, A. M. Kempf, Numerical study of a pulsed auto-igniting jet flame with detailed tabulated chemistry, Fuel 252 (2019) 408–416.

[9] C. M. Arndt, J. D. Gounder, W. Meier, M. Aigner, High-speed imaging of auto-ignition of pulsed methane jets in a hot vitiated co-flow, App. Phy. B 108 (2) (2012) 407–417.

[10] C. M. Arndt, R. Schießl, J. D. Gounder, W. Meier, M. Aigner, Flame stabilization and auto-ignition of pulsed methane jets in a hot coflow: Influence of temperature, Proc. Combust. Inst. 34 (1) (2013) 1483–1490.

[11] M. J. Papageorge, C. M. Arndt, F. Fuest, W. Meier, J. A. Sutton, High–speed mixture fraction and temperature imaging of pulsed, turbulent fuel jets auto-igniting in high-temperature, vitiated co-flows, Exp. Fluids 55 (7) (2014) 1763–1783.

[12] C. M. Arndt, M. J. Papageorge, F. Fuest, J. A. Sutton, W. Meier, M. Aigner, The role of temperature, mixture fraction, and scalar dissipation rate on transient methane injection and auto-ignition in a jet in hot coflow burner, Combust. Flame 167 (2016) 60–71.

[13] M. J. Papageorge, C. M. Arndt, F. Fuest, W. Meier, J. A. Sutton, Erratum to: High–speed mixture fraction and temperature imaging of pulsed, turbulent fuel jets auto-igniting in high-temperature, vitiated co-flows, Exp. Fluids 57 (1) (2016) 14–20.

[14] B. B. Dally, A. Karpetis, R. Barlow, Structure of turbulent non-premixed jet flames in a diluted hot coflow, Proc. Combust. Inst. 29 (1) (2002) 1147–1154.

[15] E. Oldenhof, M. Tummers, E. van Veen, D. Roekaerts, Role of entrainment in the stabilisation of jet-in-hot-coflow flames, Combust. Flame 158 (8) (2011) 1553–1563.

[16] A. Fiolitakis, P. Ess, P. Gerlinger, M. Aigner, Anwendung eines Transportgleichungs-PDF-Verfahrens zur Berechnung der Selbstzündung eines Methan-Freistrahles, 27. Deutscher Flammentag, 2015.

[17] B. Liu, J. An, F. Qin, R. Li, G.-Q. He, L. Shi, D. Zhang, Large eddy simulation of auto-ignition kernel development of transient methane jet in hot co-flow, Combust. Flame 215 (2020) 342–351.

[18] A. M. Kempf, B. J. Geurts, J. C. Oefelein, Error analysis of large-eddy simulation of the turbulent non-premixed sydney bluff-body flame, Combust. Flame 158 (12) (2011) 2408–2419.

[19] E. Inanc, F. Proch, A. Kempf, Studying transient jet flames by high-resolution LES using premixed flamelet chemistry, DLES XI, Springer (2019) 237–243.

[20] G. Zhou, Numerical simulations of physical discontinuities in single and multi-fluid flows for arbitrary mach numbers, Ph.D. thesis, Chalmers Uni. of Tech., Goteborg, Sweden (1995).

[21] M. Klein, A. Sadiki, J. Janicka, A digital filter based generation of inflow data for spatially developing direct numerical or large eddy simulations, J. Comp. Phy. 186 (2) (2003) 652–665.

[22] A. M. Kempf, M. Klein, J. Janicka, Efficient generation of initial-and inflow-conditions for transient turbulent flows in arbitrary geometries, Flow, Turb. Comb. 74 (1) (2005) 67–84.

[23] T. Lu, C. K. Law, A criterion based on computational singular perturbation for the identification of quasi steady state species: A reduced mechanism for methane oxidation with no chemistry, Combust. Flame 154 (4) (2008) 761–774.

[24] S. S. Girimaji, Y. Zhou, Analysis and modeling of subgrid scalar mixing using numerical data, Phy. Fluids 8 (1996) 1224–1236.

[25] F. Nicoud, H. B. Toda, O. Cabrit, S. Bose, J. Lee, Using singular values to build a subgrid-scale model for large eddy simulations, Phy. Fluids 23 (8) (2011) 085106.

[26] B. J. Geurts, J. Fröhlich, A framework for predicting accuracy limitations in large-eddy simulation, Phy. Fluids 14 (6) (2002) L41–L44.

[27] I. B. Celik, Z. N. Cehreli, I. Yavuz, Index of resolution quality for large eddy simulations, J. Fluid Eng. 127 (5) (2005) 949–958.

[28] N. A. K. Doan, N. Swaminathan, Y. Minamoto, DNS of MILD combustion with mixture fraction variations, Combust. Flame 189 (2018) 173–189.

[29] M. U. Göktolga, J. A. van Oijen, L. P. H. de Goey, 3d DNS of MILD combustion: A detailed analysis of heat loss effects, preferential diffusion, and flame formation mechanisms, Fuel 159 (2015) 784–795.

[30] F. Proch, P. Domingo, L. Vervisch, A. M. Kempf, Flame resolved simulation of a turbulent premixed bluff-body burner experiment. part i: Analysis of the reaction zone dynamics with tabulated chemistry, Combust. Flame 180 (2017) 321–339.

[31] C. M. Arndt, Personal communication (26/11/2016).

[32] H. Pitsch, H. Steiner, Scalar mixing and dissipation rate in large-eddy simulations of non-premixed turbulent combustion, Proc. Combust. Inst. 28 (1) (2000) 41–49.

[33] D. G. Goodwin, Cantera, <code.google.com/p/cantera> (2009).

[34] G. P. Smith et al., GRI-3.0, <combustion.berkeley.edu/gri-mech> (2000).

[35] T. Kathrotia, M. Fikri, M. Bozkurt, M. Hartmann, U. Riedel, C. Schulz, Study of the H+O+M reaction forming OH*: Kinetics of OH* chemiluminescence in hydrogen combustion systems, Combust. Flame 157 (7) (2010) 1261–1273.

[36] F. Proch, A. M. Kempf, Numerical analysis of the cambridge stratified flame series using artificial thickened flame LES with tabulated premixed flame chemistry, Combust. Flame 161 (10) (2014) 2627–2646.

[37] E. S. Richardson, V. Granet, A. Eyssartier, J. Chen, Effects of equivalence ratio variation on lean, stratified methane–air laminar counterflow flames, Comb. Theo. Mod. 14 (6) (2010) 775–792.

[38] E. Inanc, N. Chakraborty, A. Kempf, Analysis of mixture stratification effects on unstrained laminar flames, Combust. Flame 219 (2020) 339–348.

[39] H. Pitsch, A C++ computer program for 0-D combustion and 1-D laminar flame calculations, RWTH Aachen (1998).

[40] N. Peters, Laminar diffusion flamelet models in non-premixed turbulent combustion, Prog. in En. Comb. Sci. 10 (3) (1984) 319–339.